ACS APPLIED NANO MATERIALS

www.acsanm.org

Article

Electronic Tongue Based on Laser-Induced Graphene Electrodes for Monitoring Ions in Aqueous Media

Rafael C. Hensel, Xavier Cetó, Osvaldo N. Oliveira,* and Manel del Valle*

Cite This: ACS Appl. Nano Mater. 2026, 9, 962−971

Read Online

ABSTRACT: This work describes the use of a portable 450 nm wavelength laser system to fabricate an electronic tongue (e-tongue) comprising an array of potentiometric laser-induced graphene (LIG) sensors on polyimide. The sensing units were modified with ion-selective polymer membranes for the detection of Ca^{2+}, Na^{+}, and K^{+}. The sensors exhibited pseudo-Nernstian behavior, with sensitivities of 32.7 ± 0.8, 63 ± 3, and 52 ± 2 mV/dec for Ca^{2+}, Na^{+}, and K^{+}, respectively, and limits of detection of 4.5 μM for Ca^{2+}, 606 μM for Na^{+}, and 66 μM for K^{+}. The qualitative response of the e-tongue was evaluated using principal component analysis (PCA), which allowed a clear distinction between monovalent and divalent ions based on the first two principal components. Discrimination among the three ions at concentrations of 20 μM, 220 μM, and 4.0 mM was achieved using the K-means clustering algorithm, with a silhouette coefficient of 0.946, close to the ideal value. Quantitative analysis using artificial neural networks (ANNs) was applied to ternary mixtures of the three ions, enabling simultaneous and accurate prediction of individual ion concentrations down to 10 μM. Furthermore, we demonstrate the capability of the e-tongue to provide reliable measurements even at trace ion concentrations in mineral water samples, confirming its suitability for precise and sensitive ion monitoring in complex, real-world applications.

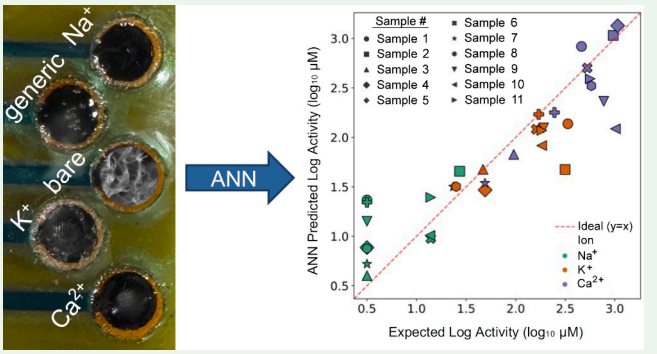

KEYWORDS: *Laser-induced graphene, Electronic tongue, Potentiometry, Sensor array, Artificial neural networks*

INTRODUCTION

The analysis of complex liquids is essential for characterizing and quantifying industrial and environmental samples. This has traditionally been performed using chromatography or other instrumental methods, which are highly efficient but require expensive equipment, controlled environments, and trained personnel.[1] There is thus a demand for simple, easy-to-use analytical techniques that are also sensitive and selective. In this context, electronic tongues (e-tongues) are an interesting alternative for analyte identification and quantification by mimicking the function of the human palate.[2−6] E-tongues combine the responses from a low-selectivity array of electrical, electrochemical, or optical sensors with machine learning or pattern recognition algorithms.[7−10] Potentiometric e-tongues, in particular, offer various advantages, including instrumental simplicity, low energy consumption, stability, and good reproducibility.[11,12] They typically use commercial liquid-junction electrodes made with ionophoric polymer membranes,[13] which are costly to produce and difficult to customize. This is why these internal liquid reference electrodes are being increasingly replaced by all-solid-state electrodes,[14] where they found applications in the industrial,[15−17] food,[18,19] pharmaceutical,[20,21] biomedical,[22] agricultural,[23] and environmental[12] fields.

E-tongues have been used for monitoring ions in water, which is relevant for environmental control, water treatment, precision agriculture, aquaculture, closed-loop water-space missions, and industrial processes. For example, a commercial potentiometric e-tongue could discriminate mineral water samples according to their geographic origin using linear discriminant analysis (LDA).[24] Five commercial drinking waters could be distinguished using principal component analysis (PCA) of the data generated with a potentiometric e-tongue comprising hollow glass and Teflon tubes containing polymer membranes.[25] The latter were made of poly(vinyl alcohol) (PVA) and poly(acrylic acid) (PAA) modified with phosphorylated hexadecyl trimethylammonium chloride, phosphorylated and cross-linked poly(vinyl-*co*-ethylene), and phosphorylated and cross-linked PVA. In another approach, ion-selective membranes (ISMs) without ionophores were plasticized into a glass ring and further incorporated into commercial ion-selective electrodes (ISEs).[18]

Received: September 23, 2025
Revised: December 10, 2025
Accepted: December 16, 2025
Published: January 2, 2026

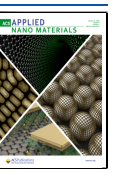

An array of six sensing units was applied to the quantitative measurement of chloride, nitrate, bicarbonate, sulfate, sodium, calcium, and magnesium in nine mineral water samples by using a straightforward linear calibration model. Despite their good prediction for Cl^-, HCO_3^-, Mg^{2+}, and Ca^{2+}, within the studied concentration ranges, the concentration of the other ions was poorly predicted. Nevertheless, the design and rigidity of sensors made from Teflon or hollow glass tubes limit their adaptability to some specific applications. To address this, the use of flow systems may be an advantage,[26] but also the use of screen-printed sensor arrays may facilitate the use.[27] As an example, Gutiérrez et al. reported a five-sensor array of screen-printed ISEs on polycarbonate substrate, which were able to quantitatively predict ammonium, potassium, and sodium concentration in real and spiked water samples by artificial neural networks (ANNs) modeling.[27] Although screen-printed ISEs are compatible with mass production, they rely on physical screens that limit their customization. Moreover, the use of carbon inks requires postprocessing for proper functioning of the sensor and may suffer from variability within distinct batches. Scalable and reproducible sensors have been produced with the automated fabrication of ISEs using printing and laser-based techniques.[28] Herein, we adopted an alternative method to fabricate an ISE-based e-tongue exploiting a more accessible, scalable, customizable, and green approach based on laser-induced graphene (LIG), which additionally takes profit of using this nanotechnology element. LIG electrodes are suitable for sensors because they can be obtained by directly scribing a substrate, providing a customized manufacture of three-dimensional graphene networks with complex designs, minimal chemical use, and waste reduction.[29−31] The e-tongue based on LIG electrodes was used for simultaneous multi-ion analysis. The working electrodes were fabricated onto polyimide using a portable 450 nm wavelength laser engraver and then coated with an intermediate layer of poly(3,4-ethylenedioxythiophene):polystyrene sulfonate (PEDOT:PSS)[32,33] and modified with poly(vinyl chloride) (PVC) ISMs. Simultaneous detection of Na^+, K^+, and Ca^{2+} was performed in deionized and mineral water samples. The data were treated with PCA and ANNs for qualitative and quantitative analyses, respectively.

MATERIALS AND METHODS

Chemicals and Solutions

Ion-selective PVC membranes were prepared using high-molecular-weight PVC and the plasticizers dioctyl sebacate (DOS), 2-nitrophenyloctyl ether (NPOE), and dioctyl phenyl phosphonate (DOPP) (all from Fluka). The ionophores valinomycin (potassium ionophore I, Fluka), bis[(12-crown-4)methyl]-2-dodecyl-2-methylmalonate (CMDMM, Dojindo Laboratories), and hemicalcium bis[4-(1,1,3,3-tetramethylbutyl)phenyl] phosphate (Ca^{2+} ionophore, Fluka) were used as recognition elements. We also used an ionophore with a generic response to cations, the dibenzo-18-crown-6 (Fluka). All membrane constituents were dissolved in tetrahydrofuran (THF, Fluka) for membrane preparation. The composition of each ISM is summarized in Table 1. The formulations of K^+ and Na^+ ISMs include 1% potassium tetrakis(4-chlorophenyl)borate as an additive. $CaCl_2{\cdot}2H_2O$, NH_4Cl, and NaCl were purchased from Panreac, and KCl and PEDOT:PSS were acquired from Merck. Goldfinger high-temperature polyimide films, 0.15 mm thick, were acquired from Henan Jinzhi Electrical Insulation New Material Co., Ltd. Green polyester high-temperature tape was purchased from Xiamen Aimo Technology Co., Ltd., and electrically conductive epoxy paste EPO-TEK E4110 was obtained from Epoxy Technology, Inc. The experiments were performed using ultrapure water obtained from a Milli-Q purification system.

Table 1. Composition of the ISMs Used to Build the LIG-Based Potentiometric Electronic Tongue[27,34]

Sensor	PVC (%)	Plasticizer (%)	Ionophore (%)
Ca^{2+}	30	DOPP - 63	7
Na^+	22	NPOE - 70	6
K^+	30	DOS - 66	3
Generic	29	DOS - 67	4

Preparation and Characterization of LIG-Based Potentiometric Sensor Array

To fabricate the LIG-based sensors, we used a portable 450 nm wavelength DAJA laser engraver (Hefei, China), model DJ6, that provides a maximum power of 3 W and a maximum resolution of 50 μm. We adjusted the engraving parameters on polyimide to fine-tune the device fabrication. The laser power, engraving speed, and focus position were varied systematically to fabricate circular LIG patterns with a diameter of 8 mm. Subsequently, the sheet resistance of the resulting graphene surfaces was evaluated using an Ossila Four-Point Probe. The morphology of the LIG surface was investigated by scanning electron microscopy using a Zeiss EVO MA10 scanning electron microscope. The quality of the LIG structures was investigated by Raman spectroscopy using a Renishaw inVia Raman microscope. The electrochemical performance of LIG-based working electrodes, having a geometric area of 12.57 mm^2, was assessed in a 0.1 M KCl solution containing 5 mM $[Fe(CN)_6]^{4-/3-}$ using a PalmSens MultiEmStat potentiostat. A combined Ag/AgCl (3 M KCl) reference and platinum counter electrode was used, along with the LIG-based working electrode. Electrochemical impedance spectroscopy (EIS) measurements were performed in a PalmSens MultiEmStat4 potentiostat by applying an AC voltage with a 10 mV amplitude at the open-circuit potential. The measurements were recorded over a frequency range of 100 kHz to 0.1 Hz.

An array of LIG electrodes on polyimide was prepared by using the optimized engraving parameters. Figure 1a presents a sketch of the engraving process. To define the active area of the electrodes, a polyester insulating tape was cut by using a 450 nm wavelength laser, as shown in Figure 1b. Then, the insulating tape was fixed onto the devices, as depicted in Figure 1c. With the aim of performing multiple measurements, robust electrical contacts were prepared by coating the LIG tracks with the conductive epoxy EPO-TEK E4110. To improve the stability of the ISEs comprising the e-tongue, reduce signal drift, and promote efficient ion-to-electron transduction, we deposited an intermediate layer of PEDOT:PSS.[33,35] 30 μL of a 10% PEDOT:PSS solution (v/v) in deionized water was drop-cast onto the LIG surface overnight at 25 °C (Figure 1d). PEDOT:PSS acts as a solid-contact material between the LIG surface and the ISM. This conductive polymer layer creates a smooth and uniform functional surface, which also improves the adhesion of the ISM. Subsequently, the sensor array was preconditioned in an aqueous solution containing 0.33 M $CaCl_2$, 0.33 M NaCl, and 0.33 M KCl for 24 h to promote the ion-exchange equilibrium of the conductive polymer layer. Before the deposition of the ion-selective membranes (ISMs), the LIG sensor array was rinsed in deionized water and left to dry overnight.

Each ISM cocktail was drop-cast on an LIG surface comprising the sensor array (Figure 1e). After the addition of each 30 μL droplet, it was left to dry for 1.5 h at 25 °C until 10 cycles were achieved. The photograph of the final array of sensors is presented in Figure 1f. Note that there is one additional sensor that was not coated by an ISM, which was used just to monitor the proper functioning of the electrodes. After the preparation of all ISEs, the sensor array was left to dry for 2 days to evaporate the solvent. The devices were subsequently preconditioned following the same procedure adopted after PEDOT:PSS deposition.

Each LIG-based ISE was characterized by the analyte addition method in Milli-Q water at 25 °C using a multichannel electronic system developed in the Sensors and Biosensors Group of UAB. This setup permits up to eight simultaneous potentiometric measurements and was coupled to a PicoLog multichannel data acquisition system (Cambridge, UK). The potentiometric measurements were performed

https://doi.org/10.1021/acsanm.5c04417
ACS Appl. Nano Mater. 2026, 9, 962−971

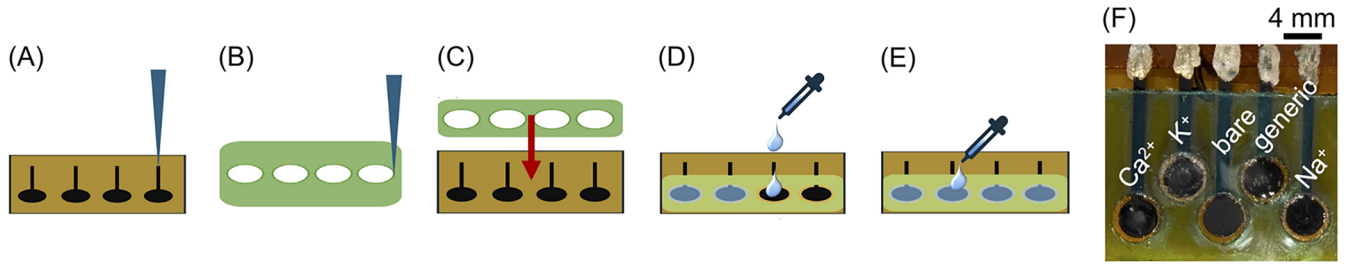

Figure 1. Sketch of the fabrication process of an LIG-based potentiometric sensor array. (A) 450 nm wavelength laser engraving of an array of electrodes having a diameter of 4 mm; (B) laser cutting of a polyester insulating tape to define the geometric area of the sensor; (C) positioning of the cut polyester insulating tape onto the electrodes; deposition of (D) PEDOT:PSS and (E) ISM onto the electrodes; and (F) photograph of the final device.

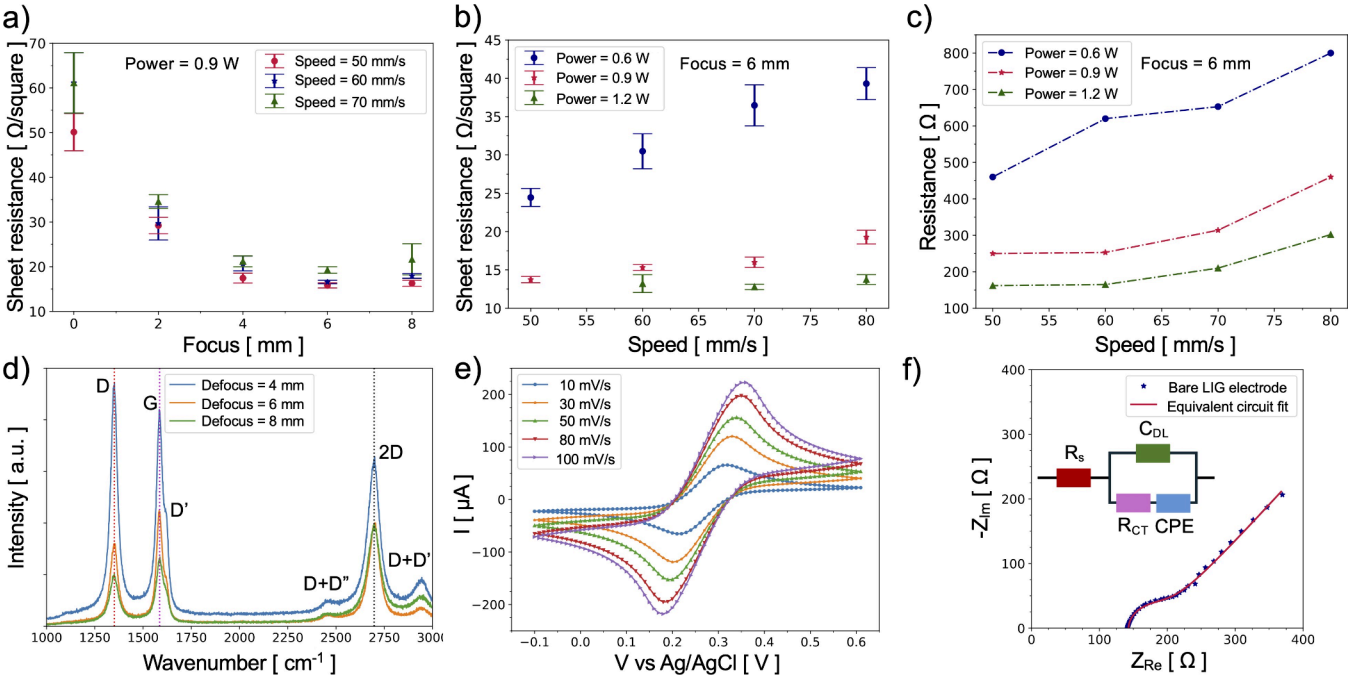

Figure 2. Sheet resistance evaluation of a circle of 4 mm radius as a function of (a) laser focus and engraving speed for a fixed laser power of 0.9 W and (b) laser power and engraving speed for a fixed defocus of 6 mm. (c) Two-probe resistance evaluation of a linear stripe of 1.1 mm × 16 mm as a function of the laser power and engraving speed for a fixed defocus of 6 mm. (d) Raman spectra of an LIG circular shape having a diameter of 8 mm engraved using a power of 0.9 W, engraving speed of 60 mm/s, and defocus values of 4, 6, and 8 mm. (e) Cyclic voltammetry curves of LIG electrodes at different scan rates. (f) Nyquist plot of LIG electrodes; the red continuous curve corresponds to the equivalent circuit fit shown as an inset.

versus an Orion 900200 double liquid-junction Ag/AgCl reference electrode, and the system was grounded with the measuring solution through a stainless-steel wire. Following the immersion of the sensor array and reference electrode in Milli-Q water at 25 °C, the open-circuit potential was continuously recorded, while the solution was homogenized using magnetic stirring. After a few minutes, once the potential stabilized, the mean value obtained over the last 20 s was taken as the baseline. Subsequently, after each analyte addition, the open-circuit potential was continuously recorded, and the same time window was used to define each measurement. To avoid drifts and recalibration, each analyte measurement was subtracted from the baseline value obtained in the presence of only Milli-Q water. At the end of the experiment, the sensors were rinsed with Milli-Q water for a few minutes to remove the residual species.

The sensor array comprising the electronic tongue was initially evaluated for three distinct concentrations of each analyte, i.e., 20 μM, 220 μM, and 4 mM, considering seven independent measurements for each sample and following the methodology described above. It is important to highlight that after each measurement, the sensors were rinsed as described previously. The qualitative response was assessed by PCA using the machine learning software environment Orange.[36]

ANNs within the open-source machine learning library PyTorch for Python[37−39] were used to quantitatively evaluate the performance of the LIG-based potentiometric electronic tongue. For their training, two complete factorial design and additional cross-validation sample datasets were implemented. Each design included three analytes at three concentrations, supplemented by three additional single-analyte samples, resulting in a total of 60 training samples, as shown in Table S2 in the Supporting Information (SI). Twenty-two additional samples randomly defined were used to externally validate the ANN model (Table S3 in the SI). In addition, four commercial mineral water samples were analyzed to predict their ion concentrations using the trained ANN. Details regarding the source and composition are provided in the SI. The order in which the measurements were performed was randomly defined to avoid any bias. The architecture of the ANN comprises an input layer, a single hidden layer with a parametrizable activation function, and a linear output layer. The most effective configuration of the ANN was identified through a grid search to define the optimal values for the hyperparameters (e.g., size of the hidden layer, activation function, learning rate, momentum, and weight decay) using PyTorch.[37−39] For each combination of hyperparameters, a new ANN instance was trained for 500 epochs using the stochastic

https://doi.org/10.1021/acsanm.5c04417
ACS Appl. Nano Mater. 2026, 9, 962−971

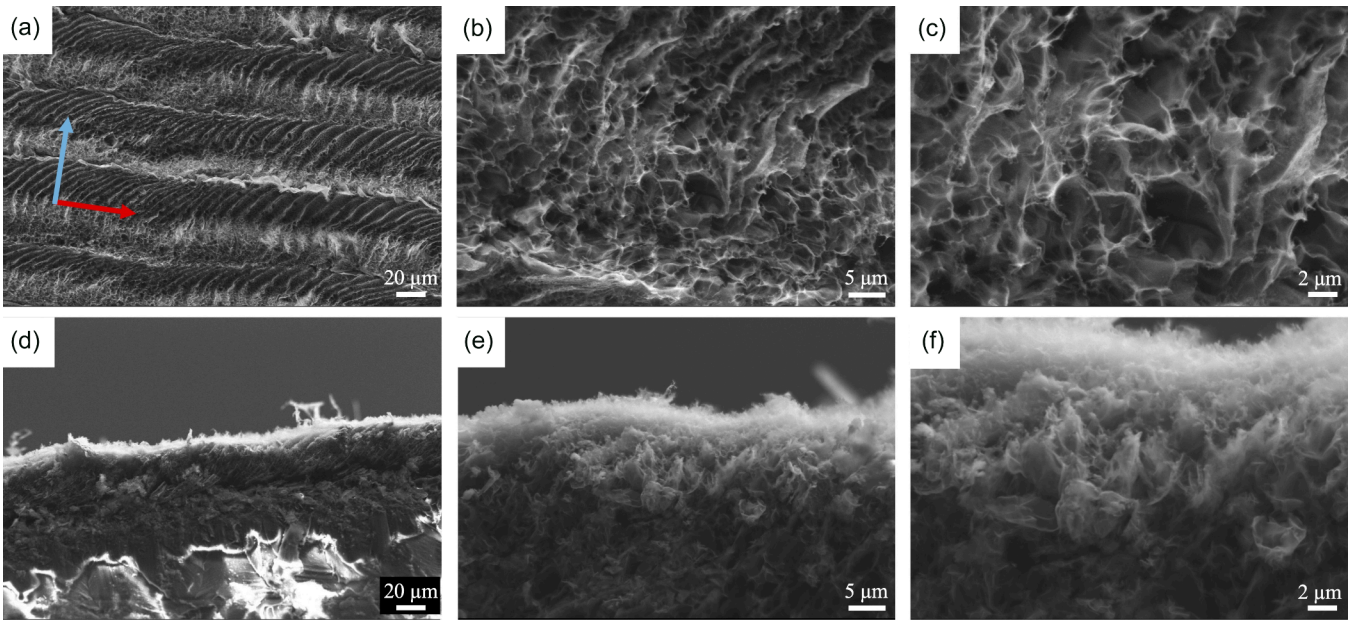

Figure 3. Top view of SEM micrographs of LIG electrodes engraved using a power of 0.9 W, engraving speed of 60 mm/s, and defocus of 6 mm at (a) 1, (b) 5, and (c) 10 k× magnification. The red arrow in (a) indicates the engraving direction. SEM micrographs of LIG electrode cross-sections at (d) 1, (e) 5, and (f) 10 k× magnification. The blue arrow is simply the orthogonal.

gradient descent (SGD) optimizer and the mean squared error loss function (MSELoss). After each configuration was trained, the model was evaluated with respect to the validation set for minimizing the validation mean squared error (MSE).

RESULTS AND DISCUSSION

Development and Characterization of LIG Electrodes

Figure 2a,b shows how the sheet resistance varies with the engraving parameters to improve the LIG performance. In Figure 2a, for a fixed laser power of 0.9 W, it was already possible to obtain a sheet resistance comparable to those reported in the literature.[40] Moreover, by lowering the engraving speed, a reduction of the size of the error bars was observed, indicating an enhancement of the fabrication reproducibility. Also, increasing the distance from the focal plane and the substrate, i.e., defocusing the laser up to 6 mm, caused a reduction of the sheet resistance, with an increasing tendency for 8 mm. Figure 2b shows that for a fixed defocus of 6 mm and a laser power of 0.6 W (blue circles), the sheet resistance increases with the engraving speed. Furthermore, the variation of the sheet resistance decreases when increasing the laser power to 0.9 W (red stars) and 1.2 W (green triangles). Nevertheless, for a laser power of 1.2 W and engraving speed of 60 mm/s, we observed that the LIG layer started to detach, which decreased the fabrication reproducibility, indicated by the increase in the size of the error bar. For the lowest scan rate tested, viz. 50 mm/s, and a laser power of 1.2 W, the devices were quite damaged, making it difficult to evaluate their sheet resistance. Therefore, the lowest sheet resistance was obtained for a laser power of 0.9 W and an engraving speed between 50 and 70 mm/s. In addition to a low sheet resistance, one must consider the conductive path of the electrodes for the sensing performance. Noble metals are normally incorporated in the conductive tracks to minimize current losses, especially in carbon-based devices.[41−43] We did not employ this metallization process but studied the dependence of the conductive track resistance as a function of the engraving parameters, as shown in Figure 2c, for conductive linear stripes of 1.1 mm × 16 mm. One can observe that increasing the engraving speed causes an increase in the resistance of the track, as indicated by the dotted lines. Also, increasing the laser power from 0.6 to 0.9 and 1.2 W reduces the resistance. Although lower resistance values were obtained for a power of 1.2 W, those patterns were quite fragile, limiting their use. Therefore, improved results were obtained with a laser power of 0.9 W and an engraving speed within 50−60 mm/s. The smaller error bars (Figure 2b) for 0.9 W are related to a more reproducible patterning.

The Raman spectra in Figure 2d feature three dominant bands at 1351, 1586, and 2698 cm^{-1}, identified as the D band, G band, and 2D band, respectively. The D band designates sp^3 carbons associated with structural defects, while the G band refers to the stretching of C−C bonds of sp^2 carbons. The 2D band is related to the scattering of two phonons with symmetric momenta in aromatic rings; thus, it provides essential information about the layer structure. Overlapped with the G band, the D′ band involves one phonon and one defect resonance, being related to distinct defects from the D band. In addition to the D′ band, the D + D′ and D + D″ bands are also defect-activated Raman features, which are common in LIG due to its partially graphitized and porous structure. For a defocus of 4 mm, I_D/I_G = 1.2, which decreased to I_D/I_G = 0.8 for a defocus of 6 mm and increased to I_D/I_G = 0.85 for 8 mm. Typically, the ratio I_D/I_G of LIG ranges between 0.6 and 1.4,[44] indicating defective but conductive networks. The lower I_D/I_G = 0.8 was obtained for a defocus of 6 mm, which agrees with the electrical characterization in Figure 2a−c. Moreover, the ratio $I_{2D}/I_G \cong 0.82$ for 4 and 6 mm defocus values indicates the presence of few-layer graphene, while $I_{2D}/I_G \cong 1.7$ for 8 mm suggests bilayer formation. Therefore, all devices used were prepared by fixing P = 0.9 W, speed = 60 mm/s, and defocus = 6 mm.

Figure 2e shows the cyclic voltammograms at diverse scan rates ν of a developed LIG device with a geometric area of 12.57 mm^2 (Figure 1f). The anodic peak at E_{pa} corresponds to the oxidation of $[Fe(CN)_6]^{4-}$ to $[Fe(CN)_6]^{3-}$, and the cathodic

https://doi.org/10.1021/acsanm.5c04417
ACS Appl. Nano Mater. 2026, 9, 962−971

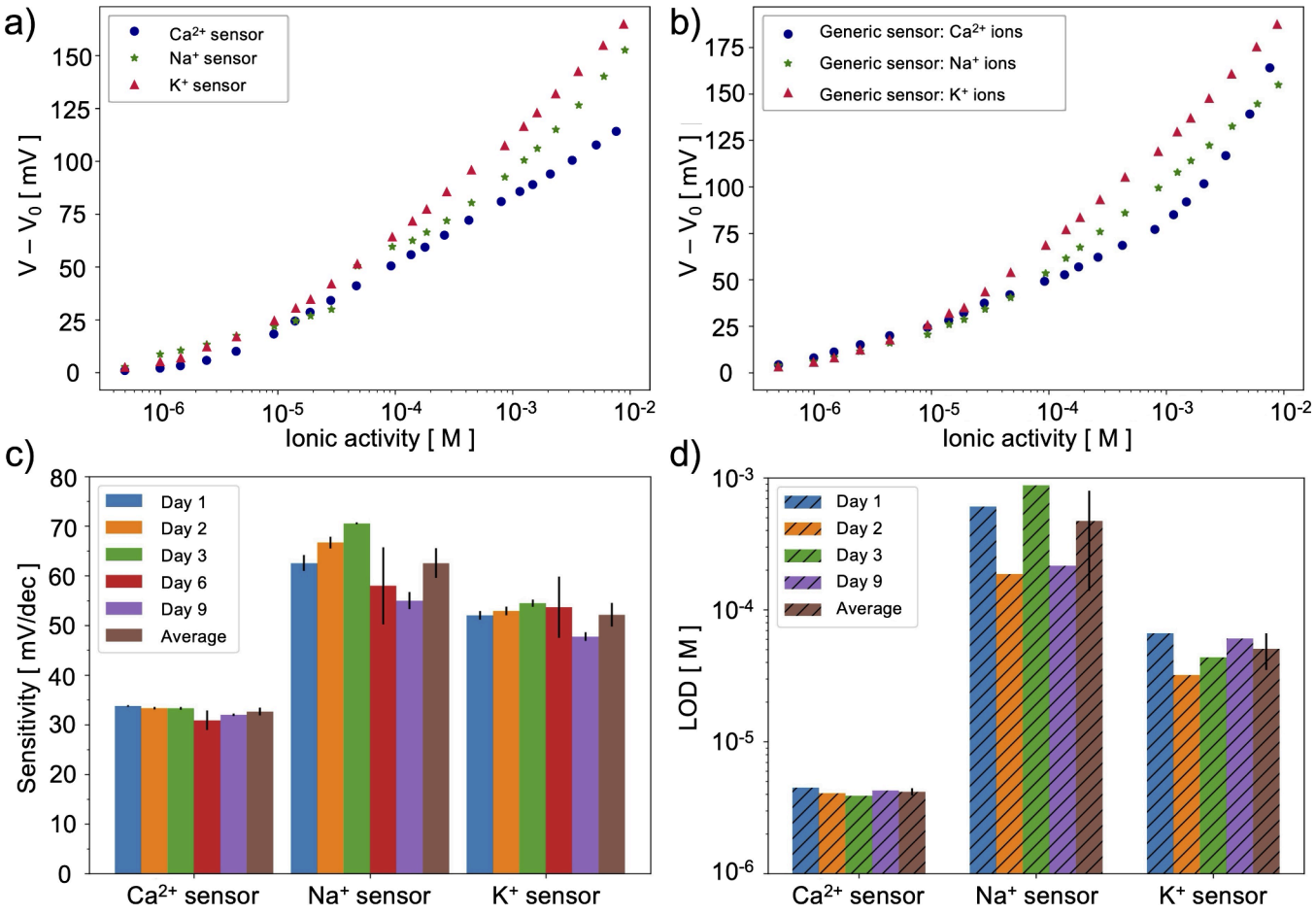

Figure 4. (a) Calibration curves of the Ca^{2+}, Na^{+}, and K^{+} ISEs with respect to the corresponding ion in Milli-Q water at 25 °C. (b) Potentiometric response of the generic sensor with respect to Ca^{2+}, Na^{+}, and K^{+} ions in Milli-Q water. (c) Sensitivity and (d) LOD evaluation of each ISE up to nine consecutive days.

peak at E_{pc} is due to the reduction of $[Fe(CN)_6]^{3-}$ back to $[Fe(CN)_6]^{4-}$. The ratio between the anodic and cathodic current peaks, i.e., $I_{pa}/I_{pc} = 1.02 \pm 0.01$, in Figure 2e is independent of the chosen scan rate. For the lowest scan rate, ν = 10 mV/s, $\Delta E_p \cong 100$ mV. This higher potential compared to that of Nernstian behavior, i.e., 59 mV, can be ascribed to ohmic drops that normally occur in these electric circuits. The linear dependence of the anodic and cathodic currents with the square root of the scan rate shown in Figure S1 in the Supporting Information indicates a diffusion-controlled process, which can be described by the Randles–Sevcik equation (eq 1). Applying eq 1 to the data in Figure S1, we calculate the active area of the LIG electrode as $A = 1.7A_{geo}$, with $R^2 = 0.9996$, while the geometric area of the devices was $A_{geo} = 0.13$ cm^2.

$$I_p = 0.4463nFAC\left(\frac{nF\nu D}{RT}\right)^{1/2} \quad (1)$$

in which I_p is the current peak [A], n is the number of electrons transferred in the redox event, A is the electrode area [cm^2], F = 96 485 C/mol is the Faraday constant, $D = 6.32 \times 10^{-6}$ cm^2/s is the diffusion coefficient, C is the concentration of the redox species [mol/cm^3], and ν is the scan rate.

The electrochemical impedance characterization of the LIG electrodes consisted of obtaining the Nyquist plots. Figure 2f features a semicircle followed by a diffusion process, which was interpreted using a modified Randles equivalent circuit, shown in the inset. The difference from the standard Randles circuit is that the Warburg element, which describes the diffusion process, was replaced by a constant phase element (CPE). The CPE is an empirical circuit element that accounts for nonideal capacitive behavior caused by surface roughness, porosity, or heterogeneity. Its impedance can be written as $Z_{CPE} = \frac{1}{Q(j\omega)^{\alpha}}$, in which Q is the constant phase element admittance, j is the imaginary number, ω is the angular frequency, and α is an empirical exponent that can assume values between 0 and 1. If $\alpha = 0$, the CPE designates a resistive component. If $\alpha = 1$, it defines a pure capacitor, and if $\alpha = 0.5$, it behaves as a Warburg element. The equivalent circuit analysis of the data in Figure 2f provided $R_s = 142 \pm 1\ \Omega$, which considers the resistance of the solution, cables, electrical contacts, etc.; $C_{DL} = 5.6 \pm 0.2\ \mu$F, which describes the double layer capacitance; $R_{CT} = 56 \pm 1\ \Omega$ for the charge transfer resistance, also correlated to the diameter of the semicircle; and $Q = (622 \pm 7) \times 10^{-6}\ s^{\alpha}/\Omega$, for $\alpha = 0.545 \pm 0.004$. Thus, as α approaches 0.5, the CPE element behaves similarly to a Warburg element. To summarize, the electrochemical characterization of the LIG devices fabricated presented results comparable to those in the literature, with the advantage of using a simpler 450 nm engraving setup.[44]

We investigated the morphology of the LIG devices by using scanning electron microscopy (SEM). Figure 3a shows a groove pattern in the direction perpendicular to the engraving one, which corresponds to a laser resolution of ~50 μm. There is a

https://doi.org/10.1021/acsanm.5c04417
ACS Appl. Nano Mater. 2026, 9, 962−971

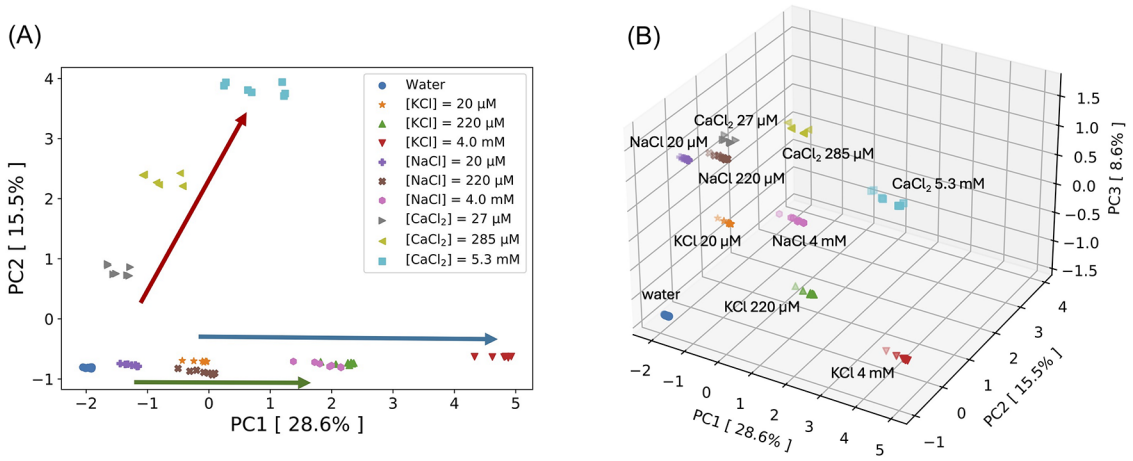

Figure 5. PCA plot for the first (A) two and (B) three principal components obtained with the e-tongue for three distinct concentrations of NaCl, KCl, and $CaCl_2$ in Milli-Q water at 25 °C.

second pattern in the engraving direction with a width of ∼10 μm that could be associated with the laser spot. Increasing the magnification, as indicated in Figure 3b,c, one notes the roughness characteristic of LIG. We have also obtained the depth profile of LIG structures using cross-sectional SEM. Figure 3d indicates that the LIG thickness is approximately 40 μm, with a foam-like structure shown in Figure 3e,f.

Potentiometric Response of LIG-Based ISEs

Figure 4a displays the comparison of the potentiometric response of the Ca^{2+}, $Na^{+,}$ and K^+ ISEs with respect to accumulated microadditions of the corresponding analyte in water, while Figure 4b shows the potential variation obtained from the generic sensor for the three analytes. Since we did not use a buffer to control the solution ionic strength, we calculated the ionic activities from the nominal molar concentrations of each ion using the extended Debye−Hückel equation to determine the activity coefficients γ, considering the ionic strength of the solution obtained after the addition of each analyte in Milli-Q water. Thus, the activity a was calculated from $a = \gamma \times c$, in which c is the molar concentration. To facilitate the comparison between different devices, all of the potentiometric measurements were presented by subtracting the initial potential value, i.e., $V - V_0$, in which V_0 corresponds to the initial measurement in Milli-Q water. In Figure 4a, there is a progressive potential increase with the initial addition of the analyte, which can be represented by two straight lines of different slopes. The small slope in the initial part of the curve occurred because the measurements were performed in deionized water instead of a buffer. The limit of detection (LOD) is defined at the intercept of the two straight lines.[14] The higher slope obeys the pseudo-Nernst equation. A similar behavior was observed for the generic ISE for the three analytes, as shown in Figure 4b. Nevertheless, in this case, the slope before reaching the pseudo-Nernstian onset was steeper, and the LOD appeared at comparatively higher analyte concentrations, a trait of its lower selectivity.

The figures of merit of the LIG-based ISEs, i.e., sensitivity and LOD, were evaluated for up to nine consecutive days as shown in Figure 4c,d, respectively. The Ca^{2+} ISE presented the lowest variation in sensitivity and LOD over the analyzed period, with an average of 32.7 ± 0.8 mV/dec and 4.2 ± 0.3 μM, respectively. Moreover, the mean sensitivity for the Na^+ and K^+ ISEs was 63 ± 3 and 52 ± 2 mV/dec, respectively. Although they present a slight deviation from pseudo-Nernstian behavior, these values are compatible with the ones already reported in the literature for screen-printed ISEs.[27] The mean value of LOD over the nine measuring days was 4.3 ± 0.4, 51 ± 16, and 401 ± 241 μM for Ca^{2+}, K^+, and Na^+, respectively. The LODs for Ca^{2+} and K^+ ISEs are similar to those presented in the literature, but the LOD for Na^+ ISE is almost 1 order of magnitude higher.[23,34,45] This may be attributed to the nonideal conditioning of the electrodes in a mixture of the three ions of interest. Such an effect is less relevant for Ca^{2+} due to the lower interference with respect to monocations.[21]

Performance of the LIG-Based E-Tongue in Qualitative Analysis

The ability of the individual LIG-based sensors to detect the ions separately serves as motivation to combine the sensing units in an e-tongue. This allowed one to distinguish the ions and even quantify them in mixtures, as will be shown next. The sensor array devised for the e-tongue was evaluated with pure solutions of one analyte, comprising three distinct concentrations of each, and seven replicate measurements for each sample. The responses of this qualitative analysis were assessed by using PCA. Figure 5a presents the bidimensional scatter plot of the obtained scores considering the first two principal components, namely PC1 and PC2. The variance explained by the first two components is below 50%, which suggests there are additional sources of variation of the measurements, for example, the existence of different monovalent cations. The readings for pure water were placed in the lower-left corner of the plot. Note that PC2 effectively separates the divalent cations from the monovalent ones, so the latter are aligned in the direction of the water samples. The red arrow indicates the direction in which samples with increasing concentrations of $CaCl_2$ were distributed. Regarding the monovalent cations, PC1 is able to separate them according to their concentration, so the green and blue arrows indicate the increasing concentration tendency for NaCl and KCl, respectively. Although the 2D plot in Figure 5a indicates an overlap between the clusters comprising 20 μM KCl and 220 μM NaCl and between 4.0 mM NaCl and 220 μM KCl, the 3D plot shown in Figure 5b permits a clearer separation according to PC3. The discrimination among the three ions and their three concentrations was also assessed by the K-means clustering algorithm, which correctly separated each sample with

https://doi.org/10.1021/acsanm.5c04417
ACS Appl. Nano Mater. 2026, 9, 962−971

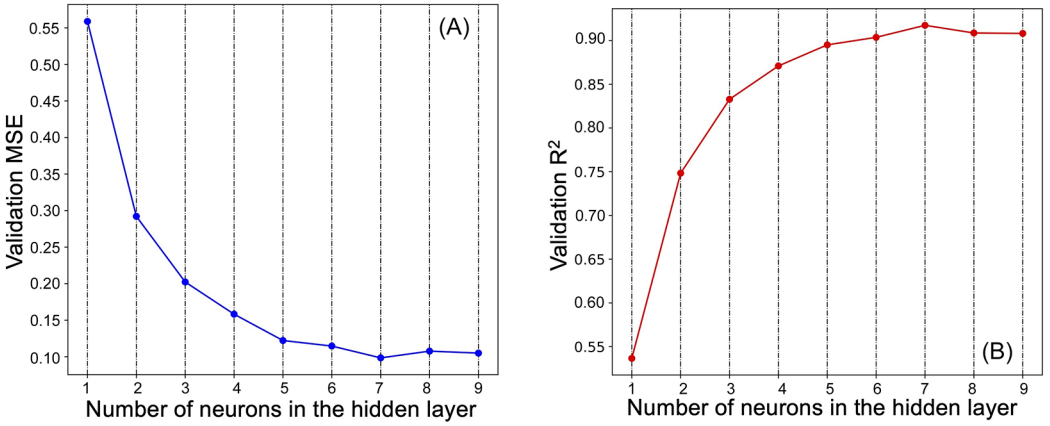

Figure 6. Optimization of the ANN configuration (A) MSE and (B) R^2 values as a function of the number of neurons in the single hidden layer to evaluate the performance of the ANN on the validation set.

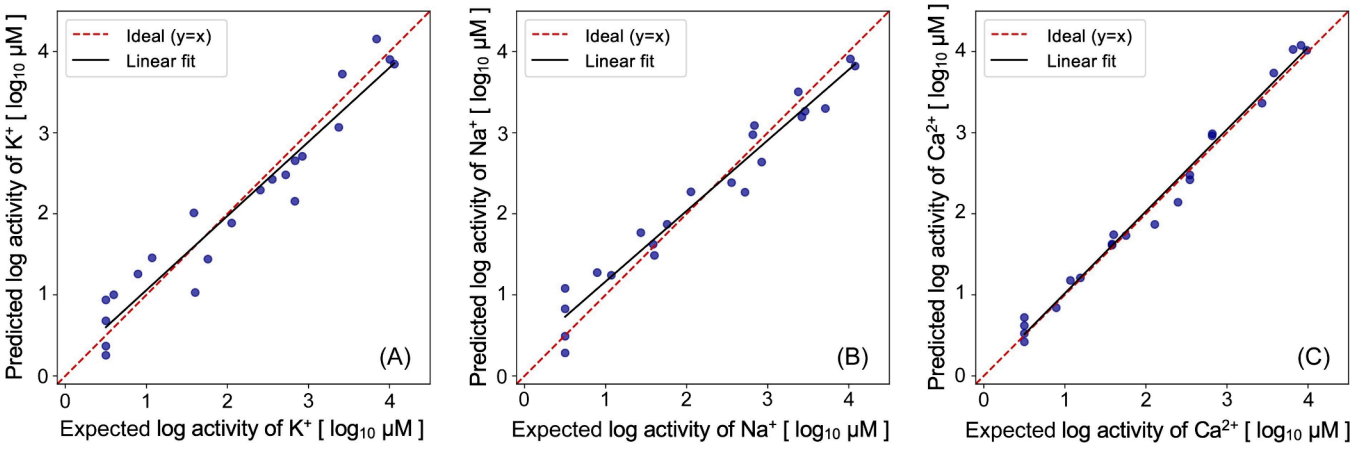

Figure 7. Predicted versus expected logarithm of the ionic activity for (A) K^+, (B) Na^+, and (C) Ca^{2+} in Milli-Q water at 25 °C on the validation set, compared with the ideal $y = x$ line and the linear fit. Obs.: The case in which the analyte is absent (i.e., 0 μM) was set to a logarithmic value of 0.5 to ensure proper data modeling and visualization.

a silhouette coefficient of 0.946, a remarkable figure close to the ideal value of 1.0.

Design and Training of the ANN Response Model

To investigate the quantitative response of the LIG-based e-tongue for the three target ions, we chose an ANN model for regression. First, the configuration was chosen with four input neurons (the number of ISEs in the array), three output neurons (the number of ions modeled), and one single hidden layer, as this has been demonstrated to be enough for similar situations.[23,27] The network topology was optimized using a grid search, as the proper choice of hyperparameters plays a crucial role in defining the ability of the ANN to capture the analytical response of the array of sensors. The design commenced by defining the fixed parameters, i.e., the number of input and output neurons. Thus, the size of the single hidden layer was varied from 1 to 10 neurons, and the learning rate was tested for 0.001, 0.01, and 0.1; the momentum for 0.0, 0.4, and 0.8; and the weight decay for 0.0, 0.001, and 0.0001. We also tested the rectified linear unit (ReLU) and tanh as the activation functions. As a result, approximately 540 distinct ANN configuration setups were evaluated, derived from a combination of $10 \times 2 \times 3 \times 3 \times 3$ hyperparameters. The ionic activity (mol/L) was converted to [μmol/L] before applying the logarithm function. This strategy optimizes the numerical range and facilitates the interpretation of the results. Moreover, to deal with the absence of an analyte, i.e., 0 M, in which the logarithm is undefined, a small arbitrary value was added to the activity before logarithmic transformation, resulting in 0.5. This ensured continuity of the mathematical validity of the data.

Figure 6 presents the validation MSE and R^2 obtained for different sizes of the hidden layer and fixed optimized parameters, namely activation function = ReLU, learning rate = 0.1, momentum = 0.4, and weight decay = 0.0001. The validation MSE decreased as the size of the hidden layer increased from 1 to 5 neurons. As the number of neurons in the hidden layer increased beyond 5, the validation MSE presented a minimum at 7 neurons, followed by a plateau up to 9 neurons. This, along with the validation R^2 values, suggests that 7 neurons offered the optimal balance between model complexity and generalization performance for this data set. It is important to highlight that the size of the hidden layer is correlated to the representation capacity of the network. Thus, a low number of neurons may not be enough to describe the data, resulting in underfitting, while a large number will cause data memorization and overfitting. This configuration provided a global validation MSE of 0.0985 and R^2 = 0.9174.

The performance of the ANN on the validation set is shown in Figure 7a–c, which presents the predicted versus the expected logarithm of the ionic activity for K^+, Na^+, and Ca^{2+}, respectively. To ensure proper data modeling and visualization on a

https://doi.org/10.1021/acsanm.5c04417
ACS Appl. Nano Mater. 2026, 9, 962−971

Table 2. Expected Concentrations and Predicted by the E-Tongue for the Three Ions in the Four Mineral Water Samples for Two Dilutions and Binary Mixtures

	Expected [K^+] (μM)	Predicted [K^+] (μM)	Expected [Na^+] (μM)	Predicted [Na^+] (μM)	Expected [Ca^{2+}] (μM)	Predicted [Ca^{2+}] (μM)
Sample 1	0	23	335	137	461	830
Sample 2	27	45	315	47	964	1073
Sample 3	0	4	47	48	95	67
Sample 4	0	8	49	29	1070	1346
Sample 5	0	22	170	171	246	179
Sample 6	14	9	161	121	526	503
Sample 7	0	5	24	32	49	35
Sample 8	0	8	25	32	580	332
Sample 9	0	14	191	125	774	232
Sample 10	14	10	183	83	1016	122
Sample 11	14	25	183	118	563	391

logarithmic scale, the case in which the analyte is absent, i.e., 0 μM, was described by an arbitrary value of 0.5, which corresponds to the lowest values in the plots. The linear regression between expected and predicted values is provided $y = (0.92 \pm 0.06)x + (0.1 \pm 0.1)$, $R^2 = 0.927$ for K^+; $y = (0.87 \pm 0.05)x + (0.3 \pm 0.1)$, $R^2 = 0.957$ for Na^+; and $y = (1.01 \pm 0.03)x - (0.01 \pm 0.05)$, $R^2 = 0.988$ for Ca^{2+}. Thus, despite the large dispersion observed for K^+ and Na^+, a unit slope and zero intercept are almost all achieved within the 95% confidence interval. Moreover, the largest deviation from ideality was obtained for K^+ and Na^+ in the absence of the target analyte in the mixture. This indicates that the model provides less reliable predictions in these low ionic activity regimes due to the lower representation of zero concentrations in the training data set.

One could also speculate as to whether the pseudo-Nernst equation, i.e., univariate application using the mean sensitivity presented in Figure 4c, could be employed for quantitative analysis of the validation set of samples. Figure S2a–c in the Supporting Information shows the comparison between the calculated versus real logarithm of the ionic activity for K^+, Na^+, and Ca^{2+}, respectively. Despite the acceptable results for Ca^{2+}, it is clear that the univariate method fails in determining the ionic activity of K^+ and Na^+. This occurred because some of the validation samples have a concentration lower than the LOD of the univariate analysis. The failures in prediction using the univariate analysis with the Nernst equation reinforce the usefulness of the ANN model for quantitative analysis.

Validation in Mineral Water

The four commercial mineral waters were diluted with Milli-Q water to concentrations of 77% and 38.5%, as described for samples 1–8 in Table 2. The concentrations of Ca^{2+}, K^+, and Na^+ in samples 1–4 were quantified by inductively coupled plasma optical emission spectrometry (ICP-OES) using an Agilent 5900 instrument, following the procedure detailed in the SI. The resulting concentrations are provided in Table S1 of the SI. Also, samples 9–11 correspond to the binary mixtures of samples 1 and 4, samples 2 and 4, and samples 2 and 3, respectively. Figure 8 presents a visual comparison between the ANN-predicted and expected logarithms of the ionic activity for K^+, Na^+, and Ca^{2+} in real samples of mineral water. As already observed in Figure 7, the ANN model cannot accurately determine the concentration of K^+ in the samples in which this ion was absent. Nevertheless, there is a good capability of predicting the concentrations of the three ions for the other samples, as presented in Table 2. Moreover, our devices performed better on the determination of K^+ and Na^+ when compared to screen-printed carbon ISEs used for the determination of these ions in real water and spiked samples.[27] It is also worth noting that the univariate analysis using the Nernst equation with the individual calibration curves was largely ineffective, as shown in Figure S3 in the Supporting Information.

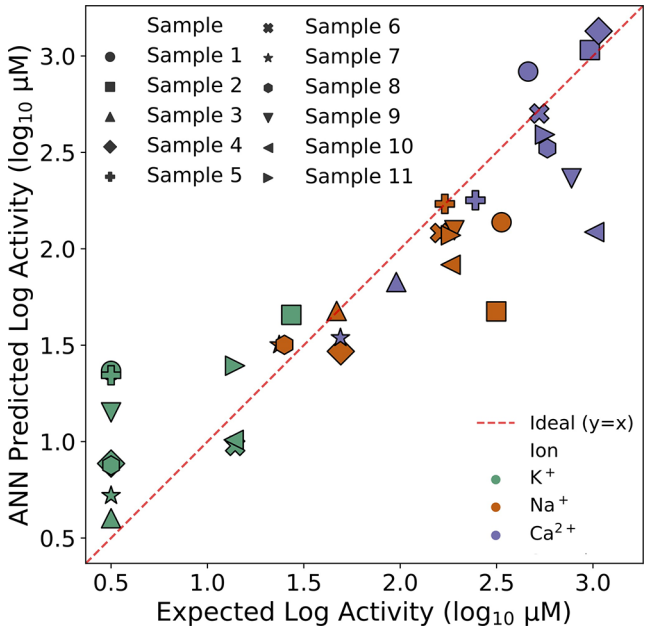

Figure 8. Comparison of ANN-predicted versus expected logarithm of the ionic activity for K^+, Na^+, and Ca^{2+} in real samples of mineral water diluted in Milli-Q water at 25 °C, compared with the ideal $y = x$ line. Obs.: The case in which the analyte is absent (i.e., 0 μM) was set to a logarithmic value of 0.5 to ensure proper data modeling and visualization.

CONCLUSIONS

We developed an LIG-based potentiometric e-tongue, whose ability to perform multi-ion analysis in aqueous media was shown. Electrochemical characterization revealed pseudo-Nernstian behavior for the LIG-based ISEs, with stable sensitivities of 32.7 ± 0.8, 63 ± 3, and 52 ± 2 mV/dec for Ca^{2+}, Na^+, and K^+, respectively, over nine days. PCA successfully distinguished between monovalent and divalent cations, also indicating concentration-dependent trends. Moreover, K-means clustering provided a silhouette coefficient of 0.946, which indicates excellent classification of the three concentrations of the three ions. Quantitative analysis performed with ANNs

https://doi.org/10.1021/acsanm.5c04417
ACS Appl. Nano Mater. 2026, 9, 962–971

demonstrated good predictive performance in estimating the logarithm of ionic activity of the three ions, indicated by the regression parameters closely matching the unit slope and zero intercept within the 95% confidence interval. This indicates that the ANN output remained statistically consistent with the expected behavior. Furthermore, the network successfully learned the underlying relationship between the sensor array inputs and the ionic activity values for K^+, Na^+, and Ca^{2+} in real mineral water samples. To be noted was the systematic deviation in the prediction of K^+ for samples that did not contain K^+ ions, which may also have affected the overall predictive accuracy of the model. Overall, these results highlight the feasibility of integrating LIG-based potentiometric sensors into flexible and miniaturized e-tongue platforms for advanced chemical sensing, also opening perspectives for wearable applications.

■ ASSOCIATED CONTENT

Supporting Information

The Supporting Information is available free of charge at https://pubs.acs.org/doi/10.1021/acsanm.5c04417.

Details regarding the source and composition of the mineral water samples; concentration of ions in commercial mineral water samples; composition of the 60 solutions that formed the randomly defined ANN training set; composition of the 22 solutions comprising the randomly selected ANN validation set; linear dependence of the anodic and cathodic currents of $[Fe(CN)_6]^{4-/3-}$ with the square root of the scan rate; comparison between the calculated versus real logarithm of the ionic activity for K^+, Na^+, and Ca^{2+}, respectively, exploiting the pseudo-Nernst equation with the individual calibration curves; and univariate analysis of mineral water samples using the Nernst equation with the individual calibration curves (PDF)

■ AUTHOR INFORMATION

Corresponding Authors

Manel del Valle − *Sensors and Biosensors Group - Department of Chemistry, Autonomous University of Barcelona (UAB), Bellaterra, Barcelona 08193, Spain;* orcid.org/0000-0002-1032-8611; Email: manel.delvalle@uab.es

Osvaldo N. Oliveira − *Sao Carlos Institute of Physics, University of Sao Paulo (USP), Sao Carlos, SP 13566-590, Brazil;* orcid.org/0000-0002-5399-5860; Email: chu@ifsc.usp.br

Authors

Rafael C. Hensel − *Sao Carlos Institute of Physics, University of Sao Paulo (USP), Sao Carlos, SP 13566-590, Brazil; Sensors and Biosensors Group - Department of Chemistry, Autonomous University of Barcelona (UAB), Bellaterra, Barcelona 08193, Spain;* orcid.org/0000-0001-7060-6604

Xavier Cetó − *Sensors and Biosensors Group - Department of Chemistry, Autonomous University of Barcelona (UAB), Bellaterra, Barcelona 08193, Spain*

Complete contact information is available at: https://pubs.acs.org/10.1021/acsanm.5c04417

Author Contributions

The manuscript was written through contributions of all authors. All authors have given approval to the final version of the manuscript.

Funding

This work was supported by INEO, CNPq, CAPES and FAPESP (2018/22214-6, 2020/15095-0, 2023/07812-2), and by MCIN/AEI/10.1303/501100011033, through the project PID2022-136709OB-C21 and the network Electrobionet (RED2022-134120-T).

Notes

The authors declare no competing financial interest.

■ ABBREVIATIONS

ANNs, artificial neural networks; CMDMM, bis[(12-crown-4)methyl]-2-dodecyl-2-methylmalonate; CPE, constant phase element; DOPP, dioctyl phenyl phosphonate; DOS, dioctyl sebacate; ISE, ion-selective electrode; ISMs, ion-selective membranes; LDA, linear discriminant analysis; LIG, laser-induced graphene; LOD, limit of detection; MSE, mean squared error; MSELoss, mean squared error loss function; NPOE, 2-nitrophenyloctyl ether; PAA, poly(acrylic acid); PCA, principal component analysis; PEDOT:PSS, poly(3,4-ethylenedioxythiophene):polystyrene sulfonate; PVA, poly(vinyl alcohol); PVC, poly(vinyl chloride); ReLU, rectified linear unit; SEM, scanning electron microscopy; SGD, stochastic gradient descent; THF, tetrahydrofuran

■ REFERENCES

(1) Nez, O.; Gallart-Ayala, H.; Martins, C. P.B.; Lucci, P. New Trends in Fast Liquid Chromatography for Food and Environmental Analysis. *J. Chromatogr A* **2012**, *1228*, 298−323.

(2) Riul, A., Jr.; Dantas, C. A. R.; Miyazaki, C. M.; Oliveira, O. N., Jr. Recent Advances in Electronic Tongues. *Analyst* **2010**, *135* (10), 2481−2495.

(3) del Valle, M. Electronic Tongues Employing Electrochemical Sensors. *Electroanalysis* **2010**, *22* (14), 1539−1555.

(4) Łabańska, M.; Ciosek-Skibińska, P.; Wróblewski, W. Critical Evaluation of Laboratory Potentiometric Electronic Tongues for Pharmaceutical Analysis—an Overview. *Sensors* **2019**, *19* (24), 5376.

(5) Ciosek, P.; Wróblewski, W. Potentiometric and Hybrid Electronic Tongues for Bioprocess Monitoring − an Overview. *Anal. Methods* **2015**, *7* (9), 3958−3966.

(6) Rudnitskaya, A.; Lvova, L. Chapter 32 - Gustatory-Based Electronic Tongues. In *Nature-Inspired Sensors*; Haick, H., Ed.; Elsevier, 2025; pp 467−486. DOI: 10.1016/B978-0-443-15684-7.00037-3.

(7) Shimizu, F. M.; Braunger, M. L.; Riul, A. Heavy Metal/Toxins Detection Using Electronic Tongues. *Chemosensors* **2019**, *7* (3), 36.

(8) Han, F.; Zhang, D.; Rashed, M. M. A.; Dai, C.; Zhang, X.; Jiang, B.; Zhang, X.; Huang, X. Machine Learning-Enhanced Taste Sensing for Dual Additive Quantification: Simultaneous Salt and MSG Prediction in Complex Food Liquid. *Food Bioproc Tech* **2025**, *18*, 8569−8584.

(9) Shojaeifard, Z.; Moslehipour, A.; Hemmateenejad, B. Chapter 5 - Optical and Electronic Nose and Tongue. In *Nature-Derived Sensors*; Hemmateenejad, B., Altintas, Z., Rafatmah, E., Eds.; Elsevier, 2025; pp 173−200. DOI: 10.1016/B978-0-443-22002-9.00010-5.

(10) Han, F.; Huang, X.; Teye, E. Novel Prediction of Heavy Metal Residues in Fish Using a Low-Cost Optical Electronic Tongue System Based on Colorimetric Sensors Array. *J. Food Process Eng.* **2019**, *42* (2), No. e12983.

(11) Cho, S.; Moazzem, M. S. Recent Applications of Potentiometric Electronic Tongue and Electronic Nose in Sensory Evaluation. *Prev Nutr Food Sci.* **2022**, *27* (4), 354−364.

(12) Mimendia, A.; Gutiérrez, J. M.; Leija, L.; Hernández, P. R.; Favari, L.; Muñoz, R.; del Valle, M. A Review of the Use of the

Potentiometric Electronic Tongue in the Monitoring of Environmental Systems. *Environmental Modelling & Software* **2010**, *25* (9), 1023−1030.
(13) Durst, R. A. Ion-Selective Electrodes − The Early Years. *Electroanalysis* **2012**, *24* (1), 15−22.
(14) Criscuolo, F.; Hanitra, M. I. N.; Taurino, I.; Carrara, S.; De Micheli, G. All-Solid-State Ion-Selective Electrodes: A Tutorial for Correct Practice. *IEEE Sens J.* **2021**, *21* (20), 22143−22154.
(15) Pérez-González, C.; Salvo-Comino, C.; Martin-Pedrosa, F.; Dias, L.; Rodriguez-Perez, M. A.; Garcia-Cabezon, C.; Rodriguez-Mendez, M. L. Analysis of Milk Using a Portable Potentiometric Electronic Tongue Based on Five Polymeric Membrane Sensors. *Front Chem.* **2021**, *9*, 907460.
(16) Cetó, X.; Gutiérrez-Capitán, M.; Calvo, D.; del Valle, M. Beer Classification by Means of a Potentiometric Electronic Tongue. *Food Chem.* **2013**, *141* (3), 2533−2540.
(17) Damarla, S. K.; Zhu, X.; Kundu, M. Classification and Authentication of Mineral Water Samples Using Electronic Tongue and Deep Neural Networks. In *2021 IEEE Third International Conference on Cognitive Machine Intelligence (CogMI)*; IEEE, 2021; pp 11−16. .
(18) Cuartero, M.; Ruiz, A.; Galián, M.; Ortuño, J. A. Potentiometric Electronic Tongue for Quantitative Ion Analysis in Natural Mineral Waters. *Sensors* **2022**, *22* (16), 6204.
(19) Perez-Gonzalez, C.; Garcia-Hernandez, C.; Garcia-Cabezon, C.; Rodriguez-Mendez, M. L.; Dias, L.; Martin-Pedrosa, F. Analysis of Milk Adulteration by Means of a Potentiometric Electronic Tongue. *J. Dairy Sci.* **2024**, *107* (11), 9135−9144.
(20) Broncová, G.; Prokopec, V.; Shishkanova, T. V. Potentiometric Electronic Tongue for Pharmaceutical Analytics: Determination of Ascorbic Acid Based on Electropolymerized Films. *Chemosensors* **2021**, *9* (5), 110.
(21) Pein, M.; Kirsanov, D.; Ciosek, P.; del Valle, M.; Yaroshenko, I.; Wesoły, M.łg.; Zabadaj, M.; Gonzalez-Calabuig, A.; Wroblewski, W.; Legin, A. Independent comparison study of six different electronic tongues applied for pharmaceutical analysis. *J. Pharm. Biomed. Anal.* **2015**, *114*, 321−329.
(22) Lvova, L.; Martinelli, E.; Dini, F.; Bergamini, A.; Paolesse, R.; Di Natale, C.; D'Amico, A. Clinical Analysis of Human Urine by Means of Potentiometric Electronic Tongue. *Talanta* **2009**, *77* (3), 1097−1104.
(23) Gutiérrez, M.; Alegret, S.; Cáceres, R.; Casadesús, J.; Marfà, O.; del Valle, M. Nutrient solution monitoring in greenhouse cultivation employing a potentiometric electronic tongue. *J. Agr. Food Chem.* **2008**, *56* (6), 1810−1817.
(24) Sipos, L.; Kovács, Z.; Sági-Kiss, V.; Csiki, T.; Kókai, Z.; Fekete, A.; Héberger, K. Discrimination of Mineral Waters by Electronic Tongue, Sensory Evaluation and Chemical Analysis. *Food Chem.* **2012**, *135* (4), 2947−2953.
(25) Mahato, M.; Adhikari, B. Monitoring of Drinking Water Quality: A Preliminary Approach by an Electronic Tongue Based on Functionalized Polymer Membrane Electrodes. *Anal. Methods* **2017**, *9* (42), 6019−6031.
(26) Calvo, D.; Durán, A.; del Valle, M. Use of Sequential Injection Analysis to Construct an Electronic-Tongue: Application to Multi-determination Employing the Transient Response of a Potentiometric Sensor Array. *Anal. Chim. Acta* **2007**, *600* (1), 97−104.
(27) Gutiérrez, M.; Moo, V. M.; Alegret, S.; Leija, L.; Hernández, P. R.; Muñoz, R.; del Valle, M. Electronic Tongue for the Determination of Alkaline Ions Using a Screen-Printed Potentiometric Sensor Array. *Microchimica Acta* **2008**, *163* (1-2), 81−88.
(28) Teekayupak, K.; Lomae, A.; Agir, I.; Chuaypen, N.; Dissayabutra, T.; Henry, C. S.; Chailapakul, O.; Ozer, T.; Ruecha, N. Large-Scale Fabrication of Ion-Selective Electrodes for Simultaneous Detection of Na+, K+, and Ca2+ in Biofluids Using a Smartphone-Based Potentiometric Sensing Platform. *Microchimica Acta* **2023**, *190* (6), 237.
(29) Santos, N. F.; Pereira, S. O.; Moreira, A.; Girão, A. V.; Carvalho, A. F.; Fernandes, A. J. S.; Costa, F. M. IR and UV Laser-Induced Graphene: Application as Dopamine Electrochemical Sensors. *Adv. Mater. Technol.* **2021**, *6* (6), 2100007.
(30) Vivaldi, F.; Dallinger, A.; Poma, N.; Bonini, A.; Biagini, D.; Salvo, P.; Borghi, F.; Tavanti, A.; Greco, F.; Di Francesco, F. Sweat Analysis with a Wearable Sensing Platform Based on Laser-Induced Graphene. *APL Bioeng* **2022**, *6* (3), No. 036104.
(31) Choudhury, S.; Zafar, S.; Deepak, D.; Panghal, A.; Lochab, B.; Roy, S. S. A Surface Modified Laser-Induced Graphene Based Flexible Biosensor for Multiplexed Sweat Analysis. *J. Mater. Chem. B* **2024**, *13* (1), 274−287.
(32) Nyein, H. Y. Y.; Gao, W.; Shahpar, Z.; Emaminejad, S.; Challa, S.; Chen, K.; Fahad, H. M.; Tai, L.-C.; Ota, H.; Davis, R. W.; Javey, A. A Wearable Electrochemical Platform for Noninvasive Simultaneous Monitoring of Ca2+ and pH. *ACS Nano* **2016**, *10* (7), 7216−7224.
(33) Bobacka, J. Conducting Polymer-Based Solid-State Ion-Selective Electrodes. *Electroanalysis* **2006**, *18* (1), 7−18.
(34) Craggs, A.; Moody, G. J.; Thomas, J. D. R. Calcium Ion-Selective Electrode Measurements in the Presence of Complexing Ligands. *Analyst* **1979**, *104* (1243), 961−972.
(35) Liao, J.; Zhang, X.; Sun, Z.; Chen, H.; Fu, J.; Si, H.; Ge, C.; Lin, S. Laser-Induced Graphene-Based Wearable Epidermal Ion-Selective Sensors for Noninvasive Multiplexed Sweat Analysis. *Biosensors (Basel)* **2022**, *12* (6), 397.
(36) Orange Data Mining. https://orangedatamining.com (accessed 2025-11-11).
(37) Imambi, S.; Prakash, K. B.; Kanagachidambaresan, G. R. PyTorch. In *Programming with TensorFlow: Solution for Edge Computing Applications*; Prakash, K. B., Kanagachidambaresan, G. R., Eds.; Springer International Publishing, Cham, 2021; pp 87−104. DOI: 10.1007/978-3-030-57077-4_10.
(38) Mishra, P. Introduction to Neural Networks Using PyTorch. In *PyTorch Recipes: A Problem-Solution Approach to Build, Train and Deploy Neural Network Models*; Mishra, P., Ed.; Apress, Berkeley, CA, 2023; pp 117−133. DOI: 10.1007/978-1-4842-8925-9_4.
(39) Jagtap, A. D.; Karniadakis, G. E. How Important Are Activation Functions in Regression and Classification? A Survey, Performance Comparison, and Future Directions. *Journal of Machine Learning for Modeling and Computing* **2023**, *4* (1), 21−75.
(40) Murray, R.; Burke, M.; Iacopino, D.; Quinn, A. J. Design of Experiments and Optimization of Laser-Induced Graphene. *ACS Omega* **2021**, *6* (26), 16736−16743.
(41) Shamili, C.; Pillai, A. S.; Saisree, S; Chandran, A.; Varma, M. R.; Kuzhichalil Peethambharan, S. All-Printed Wearable Biosensor Based on MWCNT-Iron Oxide Nanocomposite Ink for Physiological Level Detection of Glucose in Human Sweat. *Biosens Bioelectron* **2024**, *258*, No. 116358.
(42) Ploner, M.; Shkodra, B.; Altana, A.; Petrelli, M.; Tagliaferri, A.; Resnati, D.; Lugli, P.; Angeli, M. A. C.; Petti, L. Flexible Electrochemical Sensor for Interleukin-6: Toward Wearable Cytokine Monitoring. *IEEE Sens Lett.* **2024**, *8* (8), 1−4.
(43) Xu, W.; Hong, L.; Zheng, J.; Li, M.; Hua, Y.; Zhao, X. Wearable Smart Sensor System for Monitoring and Intelligent Prediction of Sodium Ions in Human Perspiration. *IEEE Internet Things J.* **2024**, *11* (5), 8146−8155.
(44) Kongkaew, S.; Thipwimonmas, Y.; Hayeeabu, M.; Limbut, W. Fabrication of a 96-Electrode Array Using Carbon Dioxide Laser Ablation. *Talanta* **2024**, *274*, No. 125912.
(45) Calvo, D.; Bartrolí, J.; del Valle, M. EIS Study of Potentiometric Membranes Selective to Ca2+ Employing the New Ionophoric Antibiotic Tetronasin. *Electrochim. Acta* **2006**, *51* (8), 1569−1575.

https://doi.org/10.1021/acsanm.5c04417
ACS Appl. Nano Mater. 2026, 9, 962−971